Facile synthesis of cubic cuprous oxide for electrochemical reduction of carbon dioxide

J Mater Sci (2021) 56:1255–1271

Facile synthesis of cubic cuprous oxide for electrochemical reduction of carbon dioxide

Juqin Zeng[1,*], Micaela Castellino[2], Katarzyna Bejtka[1], Adriano Sacco[1], Gaia Di Martino[1,2], M. Amin Farkhondehfal[1], Angelica Chiodoni[1], Simelys Hernández[1,2], and Candido F. Pirri[1,2]

[1] *Center for Sustainable Future Technologies @POLITO, Istituto Italiano di Tecnologia, Via Livorno 60, 10144 Turin, Italy*
[2] *Department of Applied Science and Technology, Politecnico di Torino, C.so Duca degli Abruzzi 24, 10129 Turin, Italy*

Received: 19 April 2020
Accepted: 1 September 2020
Published online: 18 September 2020

ABSTRACT

High level of atmospheric carbon dioxide (CO_2) concentration is considered one of the main causes of global warming. Electrochemical conversion of CO_2 into valuable chemicals and fuels has promising potential to be implemented into practical and sustainable devices. In order to efficiently realize this strategy, one of the biggest efforts has been focused on the design of catalysts which are inexpensive, active and selective and can be produced through green and up-scalable routes. In this work, copper-based materials are simply synthesized via microwave-assisted process and carefully characterized by physical/chemical/electrochemical techniques. Nanoparticle with a cupric oxide (CuO) surface as well as various cuprous oxide (Cu_2O) cubes with different sizes is obtained and used for the CO_2 reduction reaction. It is observed that the Cu_2O-derived electrodes show enhanced activity and carbon monoxide (CO) selectivity compared to the CuO-derived one. Among various Cu_2O catalysts, the one with the smallest cubes leads to the best CO selectivity of the electrode, attributed to a higher electrochemically active surface area. Under applied potentials, all Cu_2O cubes undergo structural and morphological modification, even though the cubic shape is retained. The nanoclusters formed during the material evolution offer abundant and active reaction sites, leading to the high performance of the Cu_2O-derived electrodes.

Handling Editor: Kyle Brinkman.

Address correspondence to E-mail: juqin.zeng@iit.it

https://doi.org/10.1007/s10853-020-05278-y

GRAPHIC ABSTRACT

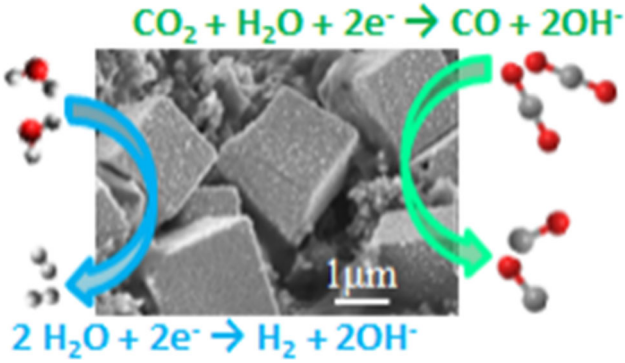

Introduction

The global energy supply based on fossil fuels has reached an unprecedented scale leading to excess anthropogenic CO_2 emission. CO_2 accumulates in the atmosphere, and its concentration has surpassed 400 ppm in 2016, much higher than the 270 ppm during the pre-industrial era [1]. As a well-known greenhouse gas, accumulated CO_2 traps more infrared radiation, breaking the energy balance on the earth's surface. Although atmospheric CO_2 concentration can be balanced by natural absorption (by the ocean and vegetation), the continuous increase in CO_2 concentration indicates that anthropogenic CO_2 emission has upset the natural balance, thus leading to global warming and climate change. Using CO_2 as feedstock to produce valuable carbon-based chemicals is considered to be a feasible approach to close the carbon cycle and mitigate the climate change. Many strategies have been developed for CO_2 valorization, including thermochemical, photochemical, electrochemical and biological approaches [2–5]. Among these methods, electrochemical CO_2 conversion is of particular interest, since it can be carried out under ambient conditions and H_2O could be the only required feedstock except CO_2. The reaction rate and the type of products can be possibly controlled by tuning the external bias and the employed electrocatalysts [1]. In addition, by using the electricity generated from renewable energy, it is possible to achieve a sustainable route for energy storage and conversion [6]. However, the carbon dioxide reduction reaction (CO_2RR) involves several proton-assisted multiple-electron-transfer processes with similar standard potentials (V versus the reversible hydrogen electrode (RHE), Reactions R1–R5) [7–9]. Moreover, H_2 evolution is the competing reaction in aqueous solution (Reaction R6). Therefore, it is a challenge to control the selectivity of the CO_2RR from the thermodynamic view:

$$CO_2 + 2H^+ + 2e^- \rightarrow CO + H_2O \quad E = -0.105\,V \tag{R1}$$

$$CO_2 + 2H^+ + 2e^- \rightarrow HCOOH \quad E = -0.169\,V \tag{R2}$$

$$CO_2 + 8H^+ + 8e^- \rightarrow CH_4 + 2H_2O \quad E = +0.169\,V \tag{R3}$$

$$2CO_2 + 12H^+ + 12e^- \rightarrow C_2H_4 + 4H_2O \quad E = +0.079\,V \tag{R4}$$

$$CO_2 + 6H^+ + 6e^- \rightarrow CH_3OH + H_2O \quad E = +0.017\,V \tag{R5}$$

$$2H^+ + 2e^- \rightarrow H_2 \quad E = 0.000\,V \tag{R6}$$

From the kinetic point of view, it is even more challenging to form chemical bonds for the complex and energetic molecule products [10]. Transferring one electron to the adsorbed CO_2 molecule to activate it (generating the radical CO_2^{*-}) is believed to be the rate-determining step of the CO_2RR on transition metal-based catalysts because of the high activation barrier needed for this step [11]. Consequently, much more negative potentials than the standard ones are

needed to drive the CO_2RR. Therefore, an appropriately designed catalyst is essential in order to activate the CO_2 molecules. Once CO_2^{*-} forms on the catalyst's surface, its reactivity in this state controls the distribution of final products. Both early and later studies [12–14] of electrochemical CO_2RR on various metal-based electrodes found that the radical CO_2^{*-} interacts with the surface of the catalyst in different ways, depending on the intrinsic electronic surface's properties of the material. Hence, a suitable catalyst is necessary in order to selectively drive the CO_2RR and to obtain a specific product.

Syngas, a mixture of H_2 and CO, can be used as an energy carrier since it can be transformed in liquid fuels through Fischer–Tropsch process or converted into other useful products such as ammonia and alcohols [15, 16]. Nowadays, syngas is mainly produced from natural gas by steam reforming, a process that requires high temperature [15]. For this reason, much effort has been devoted to developing an electrochemical process that requires less energy input, enables utilization of renewable energy and allows an easier control of H_2/CO ratio. Even though silver (Ag) and gold (Au) are the most intensively studied electrocatalysts for efficiently and selectively reducing CO_2 to CO [16], due to their high price and deficiency, many studies have been focused on other non-precious metals such as copper (Cu), zinc (Zn), tin (Sn) and bismuth (Bi) [17–20]. Due to its unique feature and high electric conductivity, Cu became the most studied element and the investigations mainly focus on size and shape effect, copper composites, copper complexes and copper alloys [21–27]. Our recent work revealed that the initial oxidation state of Cu on the surface significantly influences the performance of the catalysts in the CO_2RR [28]. A high content of Cu_2O on the as-prepared material surface improves the selectivity toward CO, while the CuO performs badly.

The present work mainly focuses on Cu_2O cubes with various sizes. We synthesized the Cu-based materials through a green route with microwave irradiation, using copper acetate as Cu precursor and ethylene glycol as solvent and reducing agent. Under the microwave radiation at 180 °C, Cu^{2+} ions were reduced, forming cubic cuprous oxide (Cu_2O) particles. The addition of Sn^{4+} ions to the copper precursor only reduced the size of Cu_2O cubes without changing the shape and oxidation state significantly, while addition of Sn^{2+} ions changed the oxidation state as well as the shape, resulting in irregular nanoparticle agglomerates. Various electrochemical techniques were applied to evaluate the activity and selectivity of these electrocatalysts toward the CO_2RR. It is revealed that the H_2/CO ratio of syngas can be easily tuned by adopting different catalysts with variations in size, shape and oxidation state.

Materials and methods

Materials

Copper acetate ($Cu(CH_3COO)_2$, 99.9%), tin(II) chloride dihydrate ($SnCl_2{\cdot}2H_2O$, 99.9%), tin(IV) chloride pentahydrate ($SnCl_4{\cdot}5H_2O$, 98%), sodium hydroxide (NaOH, 98%), potassium bicarbonate ($KHCO_3$, 99.7%), ethylene glycol (EG, 99.8%), Nafion® 117 solution (5 wt %) and isopropanol were purchased from Sigma-Aldrich. Unless otherwise specified, all the materials were used as received.

Synthesis of copper-based catalysts

The copper-based catalysts were fabricated through a microwave-assisted solvothermal route, with $Cu(CH_3COO)_2$ and $SnCl_2{\cdot}2H_2O$ or $SnCl_4{\cdot}5H_2O$ as the metal salts. The catalysts prepared with various concentrations of different salts are named as Cu(II)Sn(x)y, where x indicates the valence of Sn ions (II or IV) and y is the weight percentage (%) of Sn salt with respect to Cu one. In a typical synthesis (Scheme S1 in the Supporting Information), 900 mg of Cu salt and a certain amount of Sn salt were dissolved in 20 mL of EG to form solution 1, and 1280 mg of NaOH was dissolved in 24 mL of EG and 4 mL of H_2O to form solution 2. Then, solution 2 was added into solution 1 drop by drop. After 10 min of vigorous agitation, the mixture was then transferred into a Teflon vessel (volume 100 mL). The Teflon vessel was put in a microwave oven (Milestone STARTSynth, Milestone Inc., Shelton, Connecticut) and connected to pressure and temperature probes. The mixture was irradiated for 10 min at 180 °C (Max. 900 W) and then was cooled to ambient temperature. The precipitate was separated by centrifuge and washed twice with H_2O and once with ethanol. The powder sample was finally obtained by vacuum drying at 60 °C overnight. Three catalysts, namely Cu(II)Sn(II)5, Cu(II)Sn(IV)5 and Cu(II)Sn(IV)10, were

prepared in a solution with both Cu and Sn salts as well as a Cu(II) catalyst with only Cu precursor.

Physical/chemical characterizations

Field emission scanning electron microscopy (FESEM, ZEISS Auriga) was used to investigate the morphology. The average size of the as-prepared catalyst was evaluated based on the FESEM images taken from different areas of TEM grid. The grids were prepared by placing on them a drop of catalyst dispersed in ethanol.

X-ray diffraction (XRD) was performed in Bragg–Brentano symmetric geometry by using a PANalytical X'Pert Pro instrument (Cu-Kα radiation, 40 kV and 30 mA) equipped with an X'Celerator detector. Transmission electron microscopy (TEM) characterization was performed with a FEI Tecnai F20ST microscope, equipped with a field emission gun operating at 200 kV. The TEM samples were prepared by placing a drop of catalyst dispersed in ethanol onto a holey carbon copper grid.

X-ray photoelectron spectroscopy (XPS) was carried out by using a PHI 5000 VersaProbe (Physical Electronics) system. The X-ray source was a monochromatic Al Kα radiation (1486.6 eV). Spectra were analyzed using Multipak 9.7 dedicated software. All core-level peak energies were referenced to C1s peak at 284.5 eV, and the background contribution, in high-resolution (HR) spectra, was subtracted by means of a Shirley function.

The elemental analysis was carried out via inductively coupled plasma optical emission spectroscopy (ICP-OES), with an iCAP 7600 DUO (Thermo Fisher Scientific). The RF power of the plasma, the nebulizer gas flow, the coolant gas flow and the auxiliary gas flow were 1150 W, 0.5 L/min, 12 L/min and 0.5 L/min, respectively. Samples were weighted and digested in a flask with 10% of aqua regia overnight and filled up at volume with Milli-Q and filtered using a 0.45 µm PTFE filter before reading them with the instrument. Ar gas was used as internal standard, and the R^2 value of the calibration for the Sn and Cu elements (189.99 λ, 324.75–224.70 λ, radial mode, respectively) was 0.999.

Preparation of electrodes

To prepare the electrode, 10 mg of synthesized Cu-based catalyst (Cu(II), Cu(II)Sn(II)5, Cu(II)Sn(IV)5 or Cu(II)Sn(IV)10), 1.0 mg of acetylene carbon black (CB, Shawinigan Black AB50), 90 µL of Nafion® 117 solution and 320 µl of isopropanol were well mixed and sonicated for 30 min until a uniform slurry was obtained. The slurry was then coated onto a carbon paper (GDL; SIGRACET 28BC, SGL Technologies), which is widely used for electrode fabrication [29]. The obtained electrode was dried at 60 °C overnight to evaporate the solvents. The mass loading of Cu-based catalyst is about 3.0 mg cm^{-2}.

Electrochemical tests and reduction product analysis

Electrochemical impedance spectroscopy (EIS) measurements were performed in a three-electrode cell at room temperature with a CHI760D electrochemical workstation. The working electrode was a catalyst-coated carbon paper with a geometric area of 0.25 cm^2. A Pt wire was used as counter electrode, and Ag/AgCl (3 M NaCl) was used as reference electrode. EIS measurements were performed at various potentials from − 0.2 to − 0.8 V vs RHE with an AC signal of 10 mV of amplitude and 10^{-1}–10^4 Hz frequency range in a CO_2-saturated 0.1 M $KHCO_3$ aqueous solution. Unless otherwise specified, all the potentials refer to RHE in this work.

Chronoamperometric (CA) measurements were carried out by using a CHI760D electrochemical workstation in order to examine the electrode activity (geometric current density) and analyze the products of the CO_2RR. The CA experiments were conducted in a custom-made two-compartment cell with a proton exchange membrane (Nafion™ Membrane N117, Sigma-Aldrich) as the separator (Scheme S2). The volume of each side was 40 mL with 15 mL of headspace. Ag/AgCl (3 M NaCl) was used as the reference and a Pt foil as the counter electrode. The working electrode was composed of a catalyst (Cu(II), Cu(II)Sn(II)5, Cu(II)Sn(IV)5 or Cu(II)Sn(IV)10)-coated carbon paper with a geometric area of 1.5 cm^2. Unless specified, 0.1 M $KHCO_3$ aqueous solution was used as the electrolyte. For CA experiments, the potential was corrected by compensating the ohmic potential drop, of which 85% was corrected by the instrument (iR-compensation) and 15% by manual calculation. Gas-phase products were analyzed online with a micro-gas chromatograph (µGC, Fusion®, INFICON) equipped with two channels with a 10 m Rt-Molsieve 5A column and an 8 m Rt-Q-Bond column,

respectively, and micro-thermal conductivity detectors (micro-TCD). The inlet of the μGC was connected to the cathodic side of the electrochemical cell through a GENIE filter to remove the humidity from the gas. During the CA measurements, a constant CO_2 flow rate of 20 mL min^{-1} was maintained to saturate the electrolyte and to take the gaseous products to the μGC. Liquid products were analyzed by a high-performance liquid chromatograph (Shimadzu Prominence HPLC) with a diode array detector (DAD) set at 269 nm by using a Rezex ROA (300 × 7.8 mm) column, with 5 mM H_2SO_4 (flow rate of 0.5 mL min^{-1}) as mobile phase. The faradaic efficiency (FE) for each product was calculated by dividing the coulombs needed to produce the actual determined amount of this product by the total coulombs consumed during a corresponding reduction period.

Results and discussion

Physical and chemical characterizations

FESEM images of the synthesized Cu-based samples are shown in Fig. 1a–d. When only Cu precursor is present in the solution, cubic particles with irregular surface are obtained (Fig. 1a). On the surface of the irregular walls and close to the cubes edges, some holes, with small crystals inside (tens of nanometers), are present, evidencing the polycrystalline structure within the cube. It is important to notice that these cubes do not aggregate and show a narrow size distribution, as shown in particle size distribution histogram in Fig. 1e, with an average size of 4.0 ± 0.6 μm. When Sn(II) ions are added into the precursor solution, particles smaller in size, in the range of 30–300 nm, and with less definite shape are formed, as displayed in Fig. 1b. In addition, these irregular particles tend to form agglomerates (insert in Fig. 1b), being driven by surface energy reduction [30]. Adding Sn(IV) into the precursor solution maintains the cubic shape of the particles and increases the twinned crystals (Fig. 1c–d). It can be also observed that the surface of the cubes becomes smoother with increasing the amount of Sn(IV) ions in the solution. Compared to the Cu(II) sample, Cu(II)Sn(IV)5 and Cu(II)Sn(IV)10 have significantly reduced particle sizes, which is demonstrated by the size distribution of the cubes (Fig. 1e) and further shown at a lower magnification in Fig. S1. The average cube size of the Cu(II)Sn(IV)10 sample is of 1.7 ± 0.3 μm, slightly smaller than that of 2.1 ± 0.7 μm of the Cu(II)Sn(IV)5 sample.

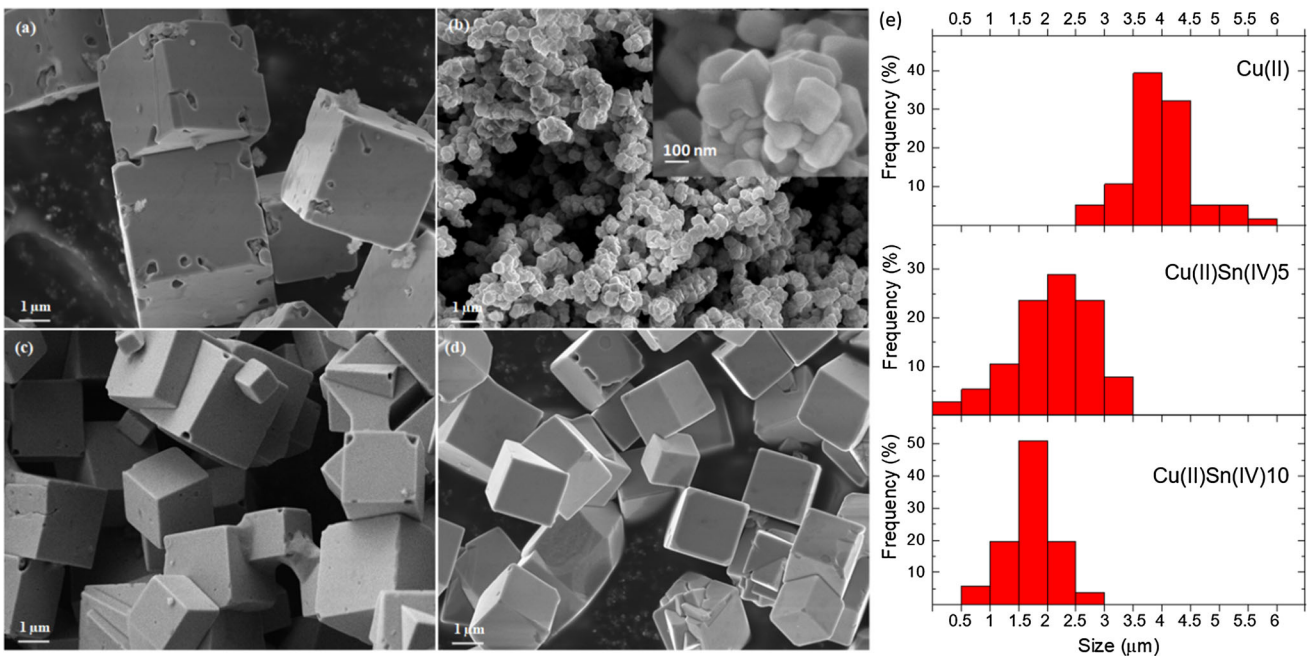

Figure 1 FESEM images of various Cu-based samples: **a** Cu(II); **b** Cu(II)Sn(II)5; **c** Cu(II)Sn(IV)5; **d** Cu(II)Sn(IV)10; and **e** particle size distribution calculated based on FESEM images for cube morphology samples.

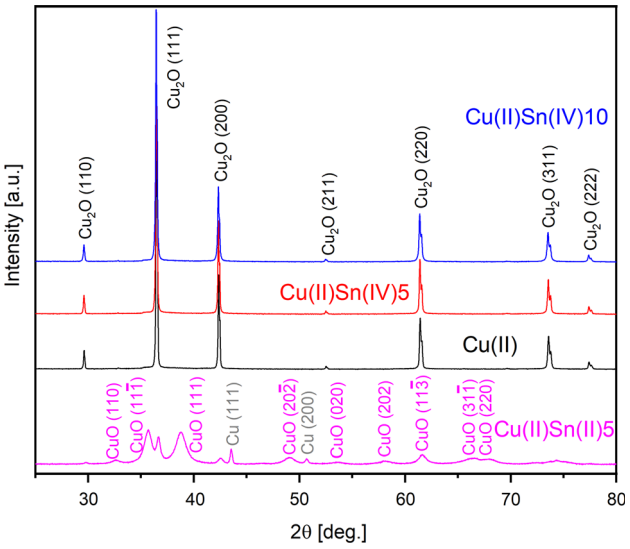

Figure 2 XRD patterns of Cu-based catalysts.

XRD patterns of Cu-based catalysts are shown in Fig. 2. For Cu(II) sample, all peaks are associated with Cu_2O and in particular to the (110), (111), (200), (211), (220), (311) and (222) planes (Cuprite, JCPDS 00-005-0667). No peaks for other crystalline phases are observed for this sample. From the XRD pattern of Cu(II)Sn(II)5 sample, the peaks related to crystalline CuO can be well observed besides those for metallic Cu (Copper, JCPDS 00-004-0836) and Cu_2O. In contrast, addition of Sn(IV) ions in the precursor solution has no effect on the crystalline phase of the samples. The Cu(II)Sn(IV)5 and Cu(II)Sn(IV)10 samples show similar XRD patterns with respect to the Cu(II) one. By applying Scherrer formula [31] to the Cu_2O (111) peak, we estimated that the coherent diffraction domain sizes are in the range of tens of nanometers for the Cu(II), Cu(II)Sn(IV)5 and Cu(II)Sn(IV)10 samples. This suggests that the Cu_2O cubes are polycrystalline, as also partially observed from FESEM, and are composed of nanosized crystallites. Small differences are found in the diffraction peak intensity ratio of (111) and (200) planes in these samples, which are 2.5, 2.8 and 3.0 for the Cu(II), Cu(II)Sn(IV)5 and Cu(II)Sn(IV)10, respectively. These values are close to the value of 2.7 reported for a standard pattern of Cu_2O with a cubic cuprite structure (Cuprite, JCPDS 00-005-0667). A gradual increase in peak intensity ratio of (111)/(200) planes indicates a slight preferential orientation for the (111) plane. This outcome could be related to the presence of twin crystals in samples with Sn(IV) ions in the precursor solution [32].

According to the literature, the (111) and (110) surfaces are thermodynamically more stable with respect to the (100) on the clean Cu_2O surfaces [33]. However, the EG molecules, as capping agents, play a crucial role during growth of Cu_2O. The binding energies of an EG molecule to the (110), (111) and (200) surfaces are variable, and a highest value is found for the EG to (200) surface from DFT calculations [28], pointing at the higher stability of the {100} surfaces in the presence of EG molecules. Hence, the growth on {100} surfaces is inhibited, while the growth along the [111] and [110] directions is unimpeded until the corresponding facets eventually disappear, explaining the appearance of cubic-shaped Cu_2O.

The TEM characterization was performed on a selected Cu(II)Sn(IV)10 sample in order to further elucidate the structural properties at the surface. The BF-TEM in Fig. 3a shows the smooth cubes walls, which is in line with what was observed by FESEM. The TEM investigation is complicated due to the large size of the cubes, which makes them only partially transparent to the electrons. The HRTEM investigation was performed by studying only edges or corners, which were the only TEM visible parts, and is shown in Fig. 3b. The observed crystalline phase is Cu_2O, which is confirmed by the fast Fourier transform (shown in the inset), and this is in agreement with the XRD observation.

In order to investigate the chemical composition of the surface of various samples, XPS measurements have been performed. From the survey spectra (not reported), Cu, O and C are the main elements. The presence of C element could be attributed to the preparation of the sample or due to adventitious carbon. Trace of Sn is also detected in the samples prepared with the presence of Sn ions in the precursor solution, as shown in Table S1. ICP-OES analysis has been performed on the as-prepared powder samples, and no trace of Sn is detected. Combining the ICP and XPS results, it is clear that Sn exists at a contamination level probably only on the surface. The Cu2*p* doublet region acquired in high-resolution (HR) mode is shown in Fig. 4a. The Cu(II), Cu(II)Sn(IV)5 and Cu(II)Sn(IV)10 samples show a typical spectrum related to the mixed oxidation states of Cu, including Cu^0, Cu^+ and Cu^{2+}, while the Cu(II)Sn(II)5 sample displays a typical spectrum

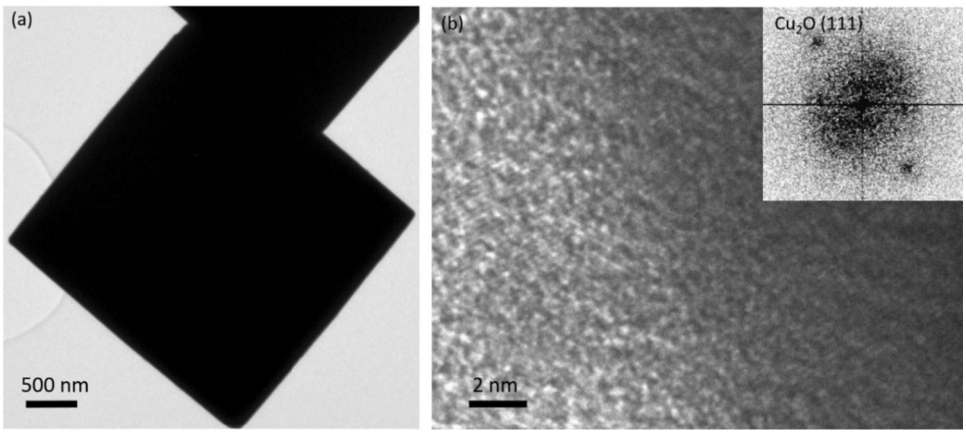

Figure 3 TEM characterization of Cu(II)Sn(IV)10 sample: **a** BF-TEM and **b** HRTEM with FFT in the inset.

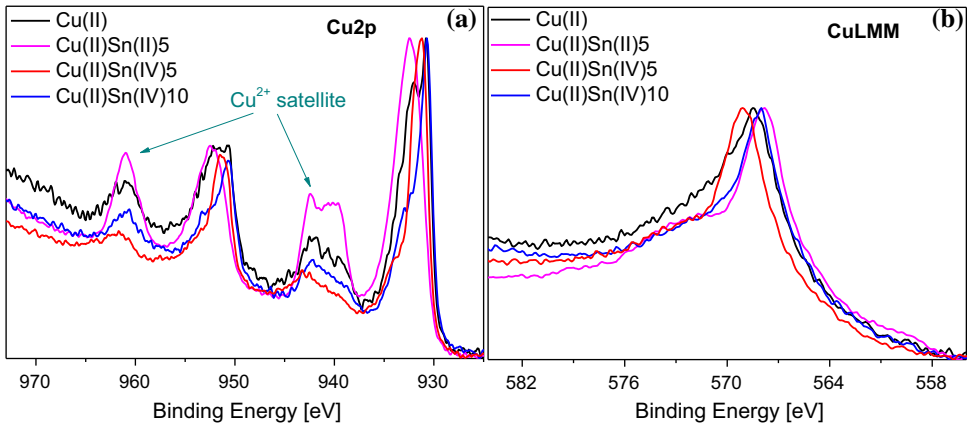

Figure 4 XPS HR spectra for Cu2*p* doublets (**a**) and Auger CuLMM region (**b**).

Table 1 Modified Auger parameter values for Cu species and relative amount of Cu(II) and Cu(0) + Cu(I) for the samples

Samples	Auger parameter (eV)	Cu^{2+} (%)	$Cu^{0} + Cu^{+}$ (%)
Cu(II)	1848.9	63	37
Cu(II)Sn(II)5	1851.3	99	1
Cu(II)Sn(IV)5	1848.7	56	44
Cu(II)Sn(IV)10	1849.3	40	60

related to only Cu^{2+} [34]. The Cu2*p* peak is complicated to be deconvoluted due to both the presence and overlapping of several satellites and shake-up peaks for each oxidation state. Hence, the Auger $CuL_3M_{4,5}M_{4,5}$ region was also acquired in order to obtain more details, as shown in Fig. 4b. The Auger parameter values are calculated according to Eq. E1 and listed in Table 1:

$$\text{Auger parameter} = h\nu - \text{CuLMM} + \text{Cu2}p_{3/2} \qquad \text{(E1)}$$

The resulting modified Auger parameter values are approximately 1849.0 eV for Cu(II), Cu(II)Sn(IV)5 and Cu(II)Sn(IV)10 samples, which corresponds to the average oxidation state (AOS) of Cu^{+} [35]. The Cu(II)Sn(II)5 sample has an average oxidation state of Cu^{2+} on the surface, indicating that its surface is mainly composed of CuO with a thickness of at least 5–10 nm (the sensible depth for XPS). To get a deeper understanding of the relative amount of Cu oxidation states, we can rely on Biesinger et al. [34] study, in which they show how to evaluate the ratio between Cu^{2+} and $Cu^{0} + Cu^{+}$, by fitting Cu2$p_{3/2}$ peak and its related satellite (Fig. 4). We have applied their formulas and obtained the values reported in Table 1. It is found that for samples Cu(II), Cu(II)Sn(IV)5 and Cu(II)Sn(IV)10 there is a variable mix of the two components with 40–63% of Cu^{2+}. On the contrary sample Cu(II)Sn(II)5 shows a quasi-total Cu^{2+} oxidation state amount (99%), in agreement with Auger parameters results.

Combining the above-mentioned analyses, we infer that the Cu(II), Cu(II)Sn(IV)5 and Cu(II)Sn(IV)10 cubes are mainly composed of crystalline Cu_2O, and their surface is made up by mixed Cu oxidation states, independent of the cube size. The Cu(II)Sn(II)5 nanoparticles have a CuO surface and contain crystalline CuO, Cu and Cu_2O phases. The absence of Sn species in the final samples is due to the conditions of the synthesis. The pH value of the final solution at the end of the synthesis is determined to be about 12.5 at room temperature. At such high pH, Sn element can be stabilized as $HSnO_2^-$ and as SnO_3^{2-} ($HSnO_2^-$/Sn, − 0.79 V; SnO_3^{2-}/$HSnO_2^-$, − 0.69 V versus SHE) [36]. These anions are soluble in H_2O or H_2O/EG and therefore are removed during washing.

CO_2RR and product analysis on the Cu-based electrodes

In order to investigate the performance of various electrodes for the CO_2RR, CA measurements were carried out in a three-electrode two-compartment cell. The concentrations of H_2 and CO were determined by μGC every 3–4 min. Liquid products were analyzed by HPLC at the end of each test. An as-prepared working electrode was used for each CA measurement. The oxides in the electrodes can be reduced under negative potentials. FESEM and XRD analyses have been performed on all Cu-based electrodes after reduction, and TEM has also been done on the reduced Cu(II)Sn(IV)10 electrode.

FESEM images in Fig. 5 show a morphology change in all electrodes after reduction. In addition to the catalysts, carbon black and Nafion binder are present as well. In the case of the samples with the cubic morphology, including Cu(II), Cu(II)Sn(IV)5 and Cu(II)Sn(IV)10, as shown in Fig. 5 a, c, d, respectively, the cubic form is preserved. However, it is clear that the surface of the cubes walls becomes rough, and is composed of small particles. After reduction, the cubes maintain similar dimensions compared to the pristine samples at the Cu(II), Cu(II)Sn(IV)5 and Cu(II)Sn(IV)10 electrodes. In the case of the electrode Cu(II)Sn(II)5 (Fig. 5b), the initial particles with very smooth surface changed to particles with rough appearance, which are actually agglomerates of much smaller particles. In addition, in all reduced Cu-based catalysts, part of the material evolved into smaller round particles. Such restructuring of the Cu-based catalysts has been widely observed under the CO_2RR conditions. Pérez-Ramírez et al. [37] reported that the electrolysis leads to a roughening of the Cu_2O catalysts, as reflected by the appearance of more defined nanometric polyhedral features on the surface of the particles. Buonsanti et al. [38] studied the morphological evolution of the Cu nanocubes during the CO_2 electrolysis and found a potential-driven nanoclustering of the cubes. They

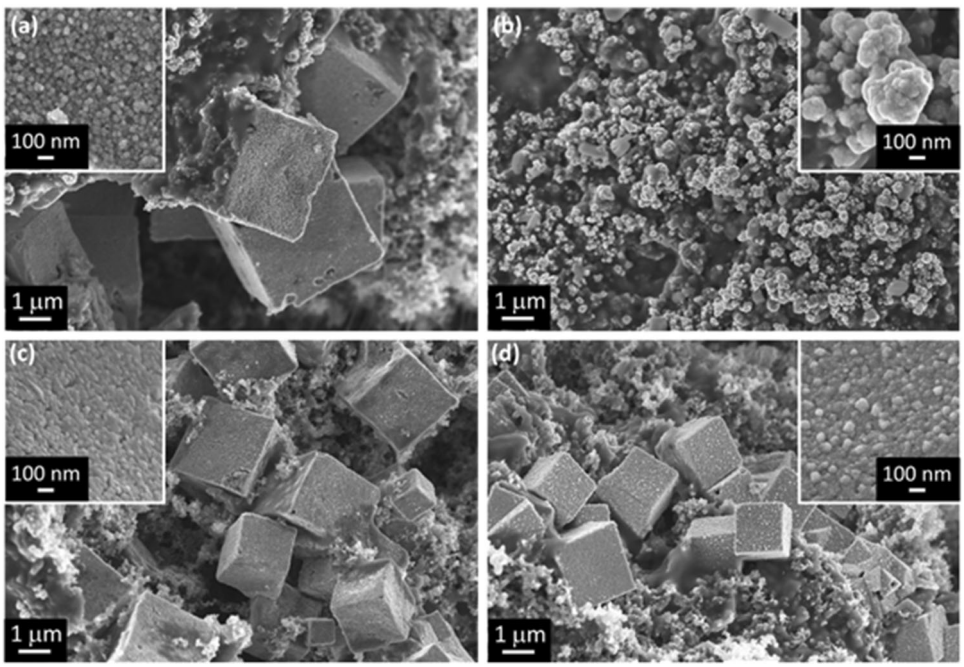

Figure 5 FESEM images of Cu-based electrodes after reduction: **a** Cu(II); **b** Cu(II)Sn(II)5; **c** Cu(II)Sn(IV)5; **d** Cu(II)Sn(IV)10.

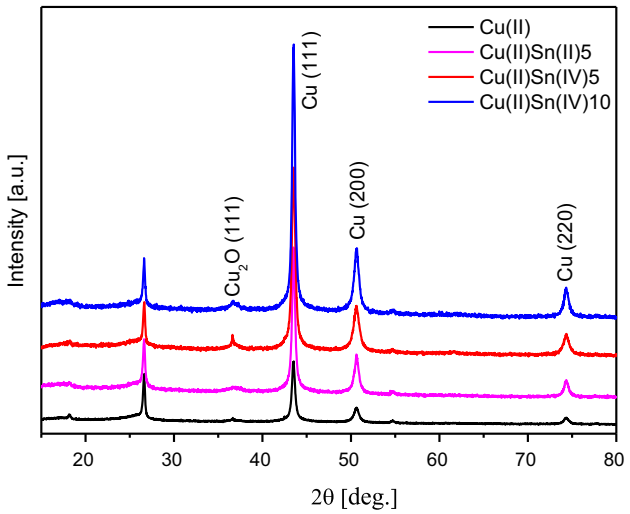

Figure 6 XRD patterns of Cu-based electrodes after reduction.

also confirmed the negative potential applied to reduce CO_2 as the main driving force for the clustering by grand-potential density functional theory calculations.

XRD patterns of the reduced electrodes are shown in Fig. 6. The peaks located at 17.9°, 26.6° and 54.7° are associated with the GDL substrate (Fig. S2). Most of CuO_x is reduced into metallic Cu after the potential is applied, while very small amount of Cu_2O is present. The crystallite size of Cu is estimated by applying Scherrer equation to the Cu(111) peak, and a similar value, in the range of tens of nanometers, has been obtained for all electrodes. This outcome confirms the nanoclustering of the electrode under applied negative potentials.

The TEM characterization of the selected Cu(II)Sn(IV)10 tested electrode was carried out in order to further elucidate the changes induced to the morphology and structure during electrochemical testing. The BF-TEM in Fig. 7a confirms that under applied negative potentials the smooth cubes walls of the untested material become rough and covered with small particles. The HRTEM of this catalyst after electrochemical testing, as shown in Fig. 7b, evidences that the small particles generated on the surface of the cubes are crystalline. This is confirmed by the FFT, in the inset, showing the ring pattern and confirming the randomly oriented crystallites. This was indexed with the lattice parameters of Cu_2O.

Even though crystalline Cu_2O is observed from XRD and TEM on the surface of the reduced electrode, we believe that the observed Cu_2O is formed due to the exposure to the air and the CuO_x is fully reduced to metallic Cu under the CO_2RR conditions. Scott et al. [39] show that the near-surface region of a polycrystalline Cu electrode is fully converted to the metallic phase at approximately + 0.3 V by live-monitoring Cu and Cu_2O Bragg peaks on the surface while scanning from open-circuit potential (OCP) to reduction potentials. Lum et al. [40] demonstrate that residual oxides are not present in significant amounts during CO_2RR through oxygen isotopic labeling of CuO_x and secondary-ion mass spectrometry measurements. Furthermore, they show that oxide-derived Cu can reoxidize rapidly, which could compromise the accuracy of ex situ methods for determining the true oxygen content. Hence, it is reasonable to consider that the CuO_x in the electrodes is fully reduced to Cu and the Cu is reoxidized in air during the sample preparation and transfer to XRD and TEM instruments.

To understand the electrochemical properties of the samples, EIS analysis has been carried out on the reduced Cu(II), Cu(II)Sn(II)5, Cu(II)Sn(IV)5 and Cu(II)Sn(IV)10 electrodes. The Nyquist spectra acquired on Cu(II)Sn(IV)10 sample at different potentials are reported in Fig. 8a. Similar spectra are

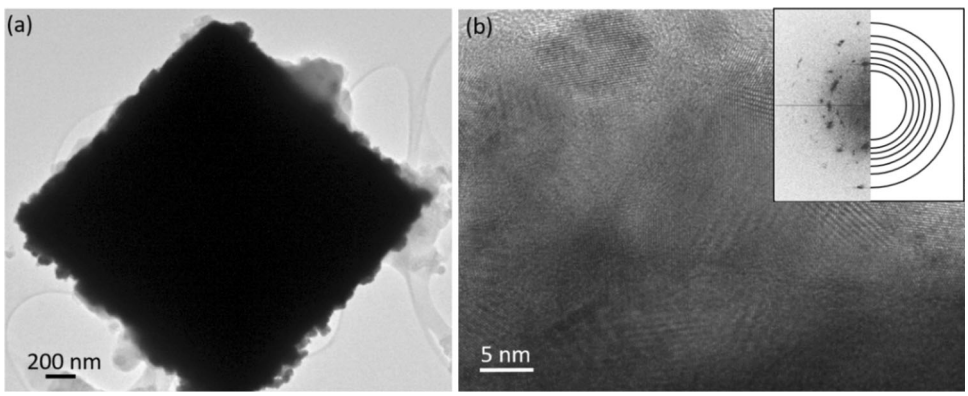

Figure 7 TEM characterization of tested Cu(II)Sn(IV)10 electrode: **a** BF-TEM and **b** HRTEM with FFT in the inset.

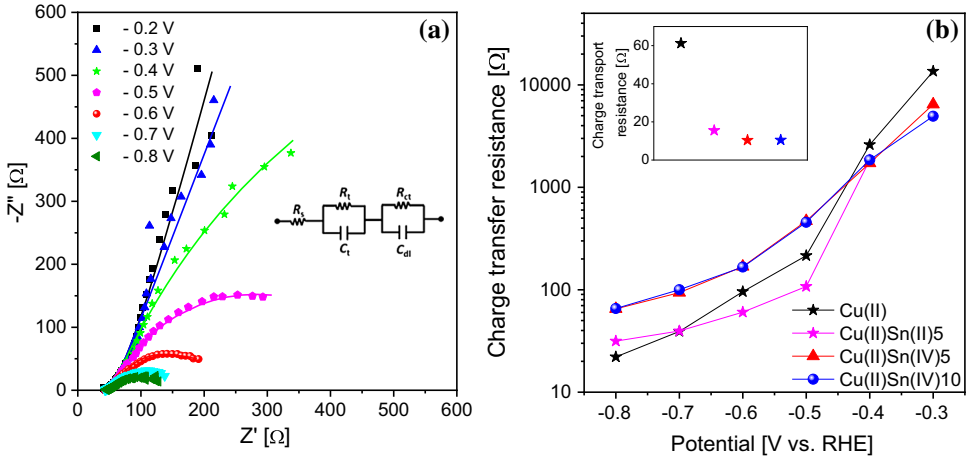

Figure 8 EIS analysis: **a** Nyquist plot of the impedance data acquired on Cu(II)Sn(IV)10 electrode in a CO_2-saturated electrolyte at different potentials (the points are experimental data, and the lines are calculated using the equivalent circuit shown in the inset); **b** charge transfer resistance and charge transport resistance (inset of **b**) obtained from the EIS fitting procedure at various electrodes. Electrode area: 0.25 cm^2.

obtained for the other electrodes, and all are constituted by two different features, which account for the charge transport inside the electrode (at high frequency, not dependent on the potential) and the charge transfer at the electrode/electrolyte interface (at low frequency, dependent on the potential) [41]. The total impedance decreases while negatively shifting the applied potential. The experimental data were fitted employing the equivalent circuit reported in the inset of Fig. 8a, in order to quantify the different resistance contributions to the total impedance. The simulated spectra, also shown in the same figure superimposed to the experimental curves, reveal a good match, thus witnessing the correct choice of the equivalent circuit. The charge transfer resistance (R_{ct}) values are reported in Fig. 8b as a function of the applied potential. Apart from the exponential behavior, it can be observed that the Cu(II) and Cu(II)Sn(II)5 samples are characterized by a smaller value with respect to the other two electrodes at each potential in the low potential range (≤ -0.5 V), while the former two displays a larger transport resistance (R_t), as shown in the inset of Fig. 8b.

Electrochemically active surface area (EASA) represents one of the most important properties of an electrode in the electrocatalysis. Besides cyclic voltammetry (CV), EIS is considered another powerful technique to determine the EASA of an electrode [42]. By fitting the EIS data, double-layer capacitance (C_{dl}) values of various electrodes are obtained and reported in Table 2. In spite of the complex nature of the electrode (composition of catalyst, carbon black and Nafion), we can reasonably estimate its EASA by comparing its C_{dl} with that of a rather flat Cu foil. This is because Cu_2O is believed to be reduced to metallic Cu in the investigated potential range as discussed above and about 90 wt% of the catalyst layer becomes metallic Cu. Waszczuk et al. [43] reported a C_{dl} value of 28 μF cm^{-2} for a flat Cu electrode. The C_{dl} values of the Cu-based electrodes are therefore divided by 28 μF cm^{-2}, resulting in the EASA of the electrodes, as listed in Table 2. The EASA values are in the following order: Cu(II) < Cu(II)Sn(IV)5 < Cu(II)Sn(IV)10 < Cu(II)Sn(II)5. It is believed that the high EASA values of the electrodes are derived from the surface roughening under the CO_2RR.

Table 2 Capacitance and EASA values of the electrodes

Electrode	C_{dl} (mF cm^{-2})	EASA (cm^2)
Cu foil	0.028	1
Cu(II)	18.72	668
Cu(II)Sn(II)5	42.35	1512
Cu(II)Sn(IV)5	20.24	722
Cu(II)Sn(IV)10	21.32	761

CO_2RR has been performed in 0.1 M $KHCO_3$ electrolyte in an H-type cell (Scheme S2). At the Cu(II) electrodes, the current densities decrease in the first 25 min due to the reduction of the catalysts and

then maintain quasi-constant, as shown in Fig. S3a. The reductive current density reaches 6.2 mA cm^{-2} at about − 0.6 V, and it increases while negatively shifting the applied potential (9.3 mA cm^{-2} at − 0.7 V and 13.6 mA cm^{-2} at − 0.9 V). The selectivity for CO formation is between 20 and 30% in this potential range, while H_2 is the main product at all potentials (Fig. S3b–d). The production rate of syngas (H_2 + CO) is about 2.6, 3.5 and 5.4 mL cm^{-2} h^{-1} at − 0.6 V, − 0.7 V and − 0.8 V, respectively. Compared to the Cu(II) electrodes, the Cu(II)Sn(II)5 ones exhibit much lower current densities at − 0.7 V and − 0.8 V (Fig. S4a) and consequently produce smaller quantity of syngas (Fig. S4b–d). Concerning the selectivity for CO, the Cu(II)Sn(II)5 electrodes have similar FE values with respect to the Cu(II) ones. The performance for the CO_2RR of Cu(II)Sn(IV)5 and Cu(II)Sn(IV)10 electrodes is shown in Fig. S5 and Fig. 9, respectively. Regarding the electrode activity, these samples show similar current densities compared to the Cu(II) ones at most potentials (Fig. S5a and 9a). However, the selectivity toward CO is significantly improved, with about 25–40% for Cu(II)Sn(IV)5 (Fig. S5b–d) and 35–50% for Cu(II)Sn(IV)10 electrodes (Fig. 9b–d).

It is worth noting that the three electrodes containing Cu_2O cubes achieve higher production rates of syngas at relatively lower overpotentials with respect to other similar studies [44, 45] and they also obtain comparable current densities with respect to the Cu-based gas diffusion electrodes (GDEs) in a flow reactor at the same potentials reported by Lan et al. [46].

Figure 10a, b summarizes the CO selectivity and H_2/CO ratios of the produced syngas, respectively. H_2 and CO are the main products at the tested potentials from − 0.6 to − 0.8 V on all electrodes. As shown in Fig. 10a, the FE_{CO} values are in the following order at each potential: Cu(II)Sn(II)5 ≈ < Cu(II) < Cu(II)Sn(IV)5 < Cu(II)Sn(IV)10. The selectivity for HCOOH remains low (FE < 10%), and no other liquid products are detected. Only CO and H_2 are detected by online μGC analysis. More negative potentials (< −0.9 V) are not recommended for syngas production on Cu-based electrodes, since other gas-phase products and C_2 liquid products can emerge, decreasing the purity and production rate of syngas [27, 46, 47]. From Fig. 10b, the H_2/CO ratio of syngas is easily tunable by using different catalysts or applying various potentials. It is interesting to note that the Cu(II)Sn(IV)10 electrodes can produce syngas with a H_2/CO ratio between 1 and 2 in all investigated potentials. This syngas is ideal for further synthesis of methanol [14].

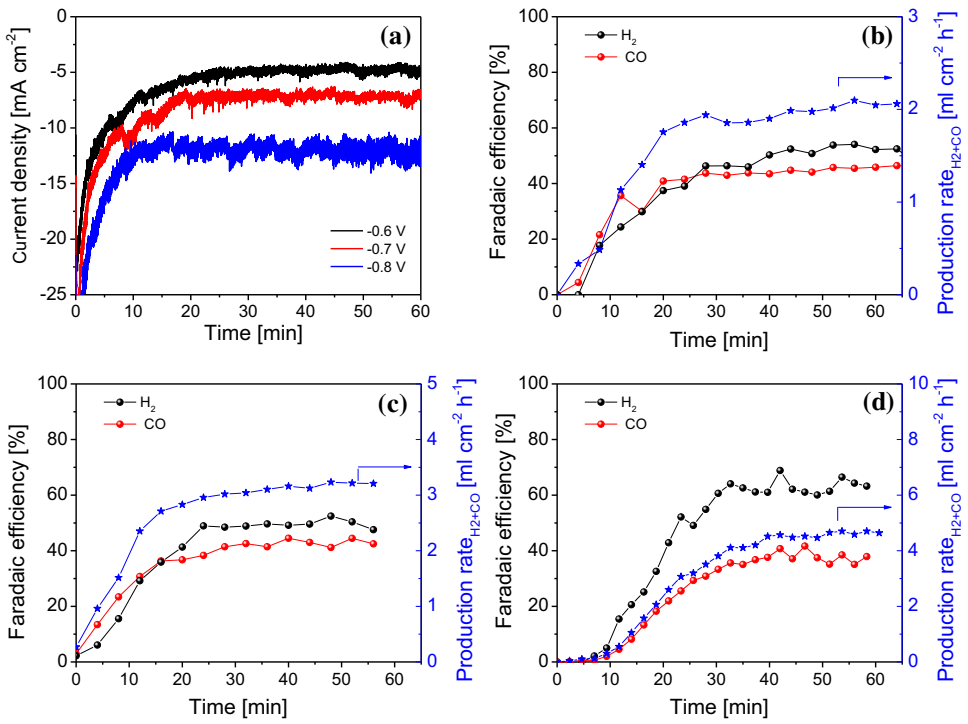

Figure 9 CA measurements on the Cu(II)Sn(IV)10 electrodes in CO_2-saturated 0.1 M $KHCO_3$ aqueous solutions at various potentials (**a**). The FE values of H_2 and CO and the production rate of syngas at various potentials: **b** − 0.6 V; **c** − 0.7 V; **d** − 0.8 V.

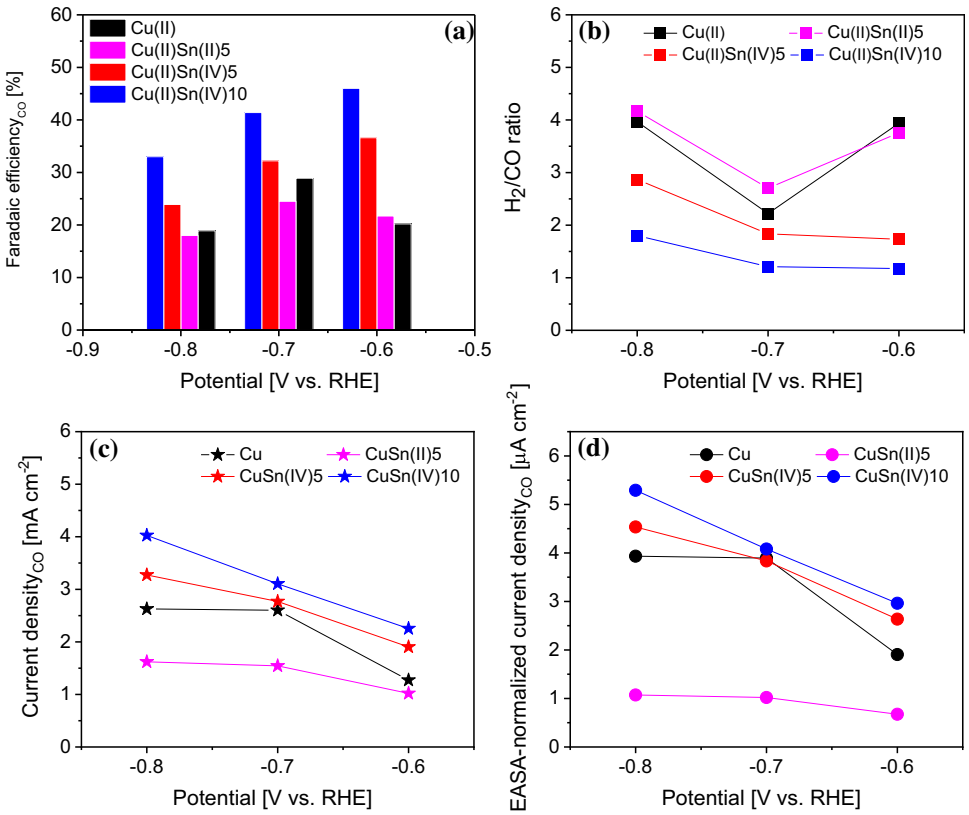

Figure 10 CO_2RR on various electrodes: faradaic efficiency for CO (**a**), the composition of the syngas (**b**), partial current density for CO formation (**c**) and EASA-normalized partial current density for CO formation (**d**). The solid lines shall guide the eye.

Partial current density for CO formation is an important parameter when evaluating the performance of an electrode for the CO_2RR to CO, since it takes into consideration both electrode activity and selectivity. The geometric partial current density for CO formation at various electrodes is compared in Fig. 10c. In general, the electrode reaches a higher CO partial current density as negatively shifting the potential. At each potential, the CO formation rate at the electrodes follows the trend: Cu(II)Sn(II)5 < Cu(II) < Cu(II)Sn(IV)5 < Cu(II)Sn(IV)10. Since the current normalized by geometric surface area of the electrode (electrode activity) does not reflect the actual activity of the catalyst, we calculated the current density normalized by the EASA listed in Table 2. It is necessary to point out the EASA values could undergo continuous change during the test since the surface roughening on the electrode could be sustained under the CO_2RR. As shown in Fig. 10d, it is clear that the Cu(II)Sn(II)5 catalyst shows much lower specific current density toward CO formation compared to other Cu_2O-derived catalysts at each potential. In addition, this CuO-derived catalyst also shows much lower specific current density for the hydrogen evolution reaction (HER), as exhibited in Fig. S6. These outcomes indicate that the reaction sites of Cu(II)Sn(II)5 catalyst could be much less active for the reduction reactions. However, it is possible that the reactions could be controlled by both kinetic and mass diffusion in the moderate-to-high overpotential range. Since the mass diffusion effect has not been taken into considerations, the specific current density could only partially reflect the intrinsic activity of the catalyst. Since both CuO and Cu_2O are considered to reduce to metallic Cu under negative potentials [39, 40], the reason of the different behaviors between the Cu_2O-derived sites and the CuO-derived ones in this work is not clear until now. It is assumed that the difference could be related to the distinct morphologies of the Cu_2O cubes and the CuO particles. Our previous work unveiled that not only the chemical composition is critical, but the morphology also plays a vital role in the CO_2 electrolysis by affecting the mass transport at the electrode/electrolyte interface [27]. Hence, in order to study the intrinsic difference between the active sites derived from Cu_2O and CuO, it is necessary to study the Cu_2O and CuO samples with similar morphology, which is not the scope of this work.

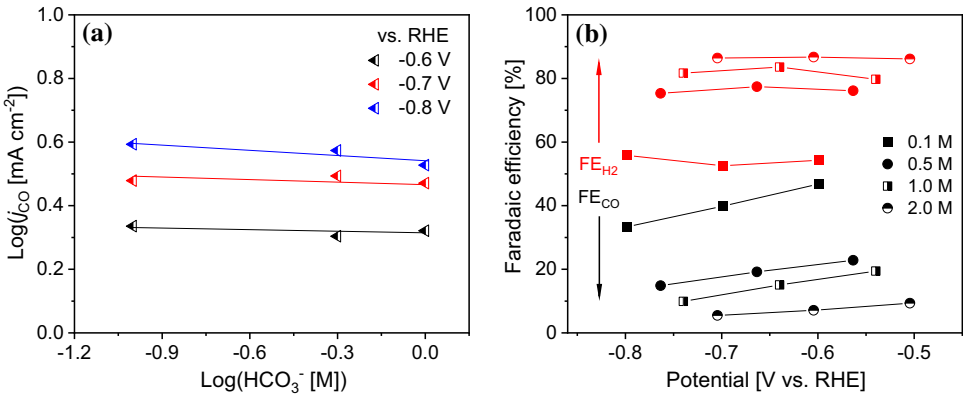

Figure 11 CO_2 electrolysis on the Cu(II)Sn(IV)10 electrode: **a** the dependence of CO partial current density on the [HCO_3^-] at logarithmic scale; **b** faradaic efficiency values for CO (black) and H_2 (red) at various potentials in electrolyte with different HCO_3^- concentrations.

From the above analyses, all three Cu_2O electrodes outperform the CuO-rich one in terms of both syngas production rate and CO selectivity. By comparison of the Cu_2O catalysts, decreasing cube size of the catalyst slightly increases the number of reaction sites and probably enhances the activity of the sites, resulting in improved performance for the CO_2RR. It is interesting to note that the three Cu_2O-derived catalysts have different trends in the H_2/CO ratio of syngas with shifting the applied potentials (Fig. 10b). Both Cu(II)Sn(IV)5 and Cu(II)Sn(IV)10 electrodes exhibit a quasi-constant H_2/CO ratio from − 0.6 to − 0.7 V and a higher ratio at − 0.8 V, while the Cu(II) is characterized by a minimum H_2/CO ratio at − 0.7 V. The lower CO selectivity of Cu(II) at − 0.6 V could be due to the slower nanoclustering at relatively positive potential due to its much bigger cube size compared to other Cu_2O samples, creating a smaller amount of active and selective sites for the CO_2RR during a determined period. The Cu(II)Sn(II)5 electrode shows a different trend, which could be attributed to the distinct behavior of its active sites for the CO_2RR.

The Cu(II)Sn(IV)10 electrodes have further been tested in $KHCO_3$ electrolyte with various concentrations. As shown in Fig. 11a, the rate of CO production is insensitive to the [HCO_3^-] at various potentials, in agreement with some recent studies on this reaction at Au and Zn electrodes [48, 49]. A zeroth-order dependence of the CO_2RR to CO rate on the [HCO_3^-] indicates that H_2O or H_3O^+ acts as the proton donor instead of HCO_3^- in the rate-limiting step of the CO_2RR [50]. Figure 11b shows higher [HCO_3^-] plays negative role in the CO_2RR to CO in terms of selectivity. As increasing the [HCO_3^-], FE_{CO} decreases, while FE_{H2} increases at each potential. This outcome is in agreement with the literature that lower bicarbonate concentrations serve to significantly enhance the CO_2RR selectivity by suppressing the HER. [48].

Conclusions

An energy-efficient route has been developed to synthesize Cu-based materials for electrochemical conversion of CO_2 to syngas. By changing the precursor solutions, it is possible to obtain catalysts with different characteristics. Cubic Cu_2O particles with various dimensions have been obtained and applied for the CO_2RR. It is revealed that the cubes undergo potential-induced crystalline and morphological modifications. These material evolutions cause dramatic surface roughing, thus creating a large number of active sites and resulting in high activity of these materials. Additionally, smaller Cu_2O cubes can achieve enhanced CO selectivity compared to the big ones, which is likely due to the increased electrochemically active surface area. Another catalyst composed of CuO/Cu/Cu_2O particles has been studied, and it shows worse selectivity for CO compared to all samples with only Cu_2O-based cubes. Hence, by employing different catalysts, syngas with various H_2/CO ratios can be easily obtained. In particular, the catalyst with the smallest Cu_2O cubes can produce syngas with a H_2/CO ratio between 1 and 2 at relatively high production rates in a wide potential range. This syngas is valuable since it has an ideal H_2/CO ratio for further methanol synthesis. The present work highlights the green synthesis of low-cost Cu-based catalysts and their potential application for large-scale CO_2 valorization.

Supporting information

Scheme of a microwave-assisted solvothermal route for preparing copper-based catalysts, scheme of a three-electrode two-compartment cell, FESEM images at low magnifications of Cu(II), Cu(II)Sn(IV)5 and Cu(II)Sn(IV)10 catalysts, XRD of a GDL substrate, detailed chronoamperometric measurements at various potentials and analyses of products on Cu(II), Cu(II)Sn(II)5 and Cu(II)Sn(IV)5 electrodes, the current density normalized by the EASA for H_2 formation at various electrodes and the XPS analysis of Cu and Sn elements on the as-prepared catalysts.

Acknowledgements

We gratefully acknowledge Dr. Filippo Drago from Istituto Italiano di Tecnologia (IIT, Genova) for performing the ICP-OES analyses.

Authors' contribution

JZ and CFP contributed to the conceptualization. SH and CFP contributed to the resources. JZ and GDM contributed to the synthesis and electrochemical measurements. MC contributed to the XPS investigation and the corresponding data analysis. KB contributed to FESEM and TEM investigations. MAF contributed to the HPLC analysis. AC contributed to the XRD investigation. AS contributed to the EIS analysis. JZ, AS and CFP contributed to the supervision of master student GDM. All authors contributed to the manuscript composition.

Funding

Open access funding provided by Istituto Italiano di Tecnologia within the CRUI-CARE Agreement.

Compliance with ethical standards

Conflicts of interest The authors declare no conflicts of interest.

Electronic supplementary material: The online version of this article (https://doi.org/10.1007/s10853-020-05278-y) contains supplementary material, which is available to authorized users.

References

[1] Wang Z-L, Li C, Yamauchi Y (2016) Nanostructured nonprecious metal catalysts for electrochemical reduction of carbon dioxide. Nano Today 11:373–391. https://doi.org/10.1016/j.nantod.2016.05.007

[2] Vickers JW, Alfonso D, Kauffman DR (2017) Electrochemical carbon dioxide reduction at nanostructured gold, copper, and alloy materials. Energy Technol 5:1–22. https://doi.org/10.1002/ente.201600580

[3] Centi G, Quadrelli EA, Perathoner S (2013) Catalysis for CO_2 conversion: a key technology for rapid introduction of renewable energy in the value chain of chemical industries. Energy Environ Sci 6:1711–1731. https://doi.org/10.1039/C3EE00056G

[4] Kondratenko EV, Mul G, Baltrusaitis J, Larrazabal GO, Perez-Ramırez J (2013) Status and perspectives of CO_2 conversion into fuels and chemicals by catalytic, photocatalytic and electrocatalytic processes. Energy Environ Sci 6:3112–3135. https://doi.org/10.1039/C3EE41272E

[5] Lim RJ, Xie MS, Sk MA, Lee JM, Fisher A, Wang X, Lim KH (2014) A review on the electrochemical reduction of CO_2 in fuel cells, metal electrodes and molecular catalysts. Catal Today 233:169–180. https://doi.org/10.1016/j.cattod.2013.11.037

[6] Kuhl KP, Hatsukade T, Cave ER, Abram DN, Kibsgaard J, Jaramillo TF (2014) Electrocatalytic conversion of carbon dioxide to methane and methanol on transition metal surfaces. J Am Chem Soc 136:14107–14113. https://doi.org/10.1021/ja505791r

[7] Zheng Y, Wang J, Yu B, Zhang W, Chen J, Qiao J, Zhang J (2017) A review of high temperature co-electrolysis of H_2O and CO_2 to produce sustainable fuels using solid oxide electrolysis cells (SOECs): advanced materials and technology. Chem Soc Rev 46:1427–1463. https://doi.org/10.1039/C6CS00403B

[8] Ganesh I (2016) Electrochemical conversion of carbon dioxide into renewable fuel chemicals: the role of nanomaterials and the commercialization. Renew Sustain Energy Rev 59:1269–1297. https://doi.org/10.1016/j.rser.2016.01.026

[9] Guzmán H, Farkhondehfal MA, Tolod KR, Hernández S, Russo N (2019) Photo/electrocatalytic hydrogen exploitation for CO_2 reduction toward solar fuels production. In: Calise F, D'Accadia MD, Santarelli M, Lanzini A, Ferrero D (eds) Solar hydrogen production. Academic Press, Cambridge, pp 365–418. https://doi.org/10.1016/B978-0-12-814853-2.00011-4

[10] Zhao G, Huang X, Wang X, Wang X (2017) Progress in catalyst exploration for heterogeneous CO_2 reduction and utilization: a critical review. J Mater Chem A 5:21625–21649. https://doi.org/10.1039/C7TA07290B

[11] Xie H, Wang T, Liang J, Li Q, Sun S (2019) Cu-based nanocatalysts for electrochemical reduction of CO_2. Nano Today 21:41–54. https://doi.org/10.1016/j.nantod.2018.05.001

[12] Hori Y, Kikuchi K, Suzuki S (1985) Production of CO and CH_4 in electrochemical reduction of CO_2 at metal electrodes in aqueous hydrogencarbonate solution. Chem Lett 14:1695–1698. https://doi.org/10.1246/cl.1985.1695

[13] Yin Z, Palmore GTR, Sun S (2019) Electrochemical reduction of CO_2 catalyzed by metal nanocatalysts. Trends Chem 8:739–750. https://doi.org/10.1016/j.trechm.2019.05.004

[14] Hernández S, Farkhondehfal MA, Sastre F, Makkee M, Saracco G, Russo N (2017) Syngas production from electrochemical reduction of CO_2: current status and prospective implementation. Green Chem 19:2326–2346. https://doi.org/10.1039/C7GC00398F

[15] Pardal T, Messias T, Sousa M, Machado ASR, Rangel CM, Nunes D, Pinto JV, Martins R, da Ponte MN (2017) Syngas production by electrochemical CO_2 reduction in an ionic liquid based-electrolyte. J CO2 Util 18:62–72. https://doi.org/10.1016/j.jcou.2017.01.007

[16] Zhu W, Zhang Y-J, Zhang H, Lv H, Li Q, Michalsky R, Peterson AA, Sun S (2014) Active and selective conversion of CO_2 to CO on ultrathin Au nanowires. J Am Chem Soc 136:16132–16135. https://doi.org/10.1021/ja5095099

[17] Zhang B, Zhang J (2017) Rational design of Cu-based electrocatalysts for electrochemical reduction of carbon dioxide. J Energy Chem 6:1050–1066. https://doi.org/10.1016/j.jechem.2017.10.011

[18] Ajmal S, Yang Y, Li K, Tahir MA, Liu Y, Wang T, Bacha A, Feng Y, Deng Y, Zhang L (2019) Zinc-modified copper catalyst for efficient (photo-)electrochemical CO_2 reduction with high selectivity of HCOOH production. J Phys Chem C 123:11555–11563. https://doi.org/10.1021/acs.jpcc.9b00119

[19] Bejtka K, Zeng J, Sacco A, Castellino M, Hernández S, Farkhondehfal MA, Savino U, Ansaloni S, Pirri CF, Chiodoni A (2019) Chainlike mesoporous SnO_2 as a well-performing catalyst for electrochemical CO_2 reduction. ACS Appl Energy Mater 2:3081–3091. https://doi.org/10.1021/acsaem.8b02048

[20] Zhang T, Qiu Y, Yao P, Li X, Zhang H (2019) Bi-modified Zn catalyst for efficient CO_2 electrochemical reduction to formate. ACS Sustain Chem Eng 18:15190–15196. https://doi.org/10.1021/acssuschemeng.9b01985

[21] Reske R, Mistry H, Behafarid F, Roldan Cuenya B, Strasser P (2014) Particle size effects in the catalytic electroreduction of CO_2 on Cu nanoparticles. J Am Chem Soc 136:6978–6986. https://doi.org/10.1021/ja500328k

[22] Sacco A, Zeng J, Bejtka K, Chiodoni A (2019) Modeling of gas bubble-induced mass transport in the electrochemical reduction of carbon dioxide on nanostructured electrodes. J Catal 372:39–48. https://doi.org/10.1016/j.jcat.2019.02.016

[23] Li Y, Cui F, Ross MB, Kim D, Sun Y, Yang P (2017) Structure-sensitive CO_2 electroreduction to hydrocarbons on ultrathin 5-fold twinned Copper nanowires. Nano Lett 17:1312–1317. https://doi.org/10.1021/acs.nanolett.6b05287

[24] Varela AS, Ju W, Bagger A, Franco P, Rossmeisl J, Strasser P (2019) Electrochemical reduction of CO_2 on metal-nitrogen-doped carbon catalysts. ACS Catal 9:7270–7284. https://doi.org/10.1021/acscatal.9b01405

[25] Hirunsit P, Soodsawang W, Limtrakul J (2015) CO_2 electrochemical reduction to methane and methanol on copper-based alloys: theoretical insight. J Phys Chem C 119:8238–8249. https://doi.org/10.1021/acs.jpcc.5b01574

[26] Zeng J, Bejtka K, Ju W, Castellino M, Chiodoni A, Sacco A, Farkhondehfal MA, Hernández S, Rentsch D, Battaglia C, Pirri CF (2018) Advanced Cu–Sn foam for selectively converting CO_2 to CO in aqueous solution. Appl Catal B 236:475–482. https://doi.org/10.1016/j.apcatb.2018.05.056

[27] Ju W, Zeng J, Bejtka K, Ma H, Rentsch D, Castellino M, Sacco A, Pirri CF, Battaglia C (2019) Sn-decorated Cu for selective electrochemical CO_2 to CO conversion: precision

architecture beyond composition design. ACS Appl Energy Mater 2:867–872. https://doi.org/10.1021/acsaem.8b01944

[28] Zeng J, Bejtka K, Di Martino G, Sacco A, Castellino M, Re Fiorentin M, Risplendi F, Farkhondehfal MA, Hernández S, Cicero G, Pirri CF, Chiodoni A (2020) Microwave-assisted synthesis of copper-based electrocatalysts for converting carbon dioxide to tunable syngas. ChemElectroChem 7:229–238. https://doi.org/10.1002/celc.201901730

[29] Zeng J, Francia C, Amici J, Bodoardo S, Penazzi N (2014) Mesoporous Co_3O_4 nanocrystals as an effective electro-catalyst for highly reversible Li–O_2 batteries. J Power Sour 272:1003–1009. https://doi.org/10.1016/j.jpowsour.2014.09.055

[30] Kim MH, Lim B, Lee EP, Xia Y (2018) Polyol synthesis of Cu_2O nanoparticles: use of chloride to promote the formation of a cubic morphology. J Mater Chem 18:4069–4073. https://doi.org/10.1039/B805913F

[31] Holder CF, Schaak RE (2019) Tutorial on powder X-ray diffraction for characterizing nanoscale materials. ACS Nano 13:7359–7365. https://doi.org/10.1021/acsnano.9b05157

[32] Kuo C-H, Huang MH (2008) Facile synthesis of Cu_2O nanocrystals with systematic shape evolution from cubic to octahedral structures. J Phys Chem C 112:18355–18360. https://doi.org/10.1021/jp8060027

[33] Soon A, Todorova M, Delley B, Stampfl C (2007) Thermodynamic stability and structure of copper oxide surfaces: a first-principles investigation. Phys Rev B 75:125420. https://doi.org/10.1103/PhysRevB.75.125420

[34] Biesinger MC, Lau LWM, Gerson AR, St R, Smart C (2010) Resolving surface chemical states in XPS analysis of first row transition metals, oxides and hydroxides: Sc, Ti, V, Cu and Zn. Appl Surf Sci 257:887–898. https://doi.org/10.1016/j.apsusc.2010.07.086

[35] Biesinger MC (2017) Advanced analysis of copper X-ray photoelectron spectra. Surf Interface Anal 49:1325–1334. https://doi.org/10.1002/sia.6239

[36] Yang T, Zhu P, Liu W, Chen L, Zhang D (2017) Recovery of tin from metal powders of waste printed circuit boards. Waste Manag 68:449–457. https://doi.org/10.1016/j.wasman.2017.06.019

[37] Larrazábal GO, Martín AJ, Krumeich F, Hauert R, Pérez-Ramírez J (2017) Solvothermally-prepared Cu_2O electrocatalysts for CO_2 reduction with tunable selectivity by the introduction of p-block elements. Chemsuschem 10:1255–1265. https://doi.org/10.1002/cssc.201601578

[38] Huang J, Hörmann N, Oveisi E, Loiudice A, De Gregorio GL, Andreussi O, Marzari N, Buonsanti R (2018) Potential-induced nanoclustering of metallic catalysts during electrochemical CO_2 reduction. Nat Commun 9:3117. https://doi.org/10.1038/s41467-018-05544-3

[39] Scott SB, Hogg TV, Landers AT, Maagaard T, Bertheussen E, Lin JC, Davis RC, Beeman JW, Higgins D, Drisdell WS, Hahn C, Mehta A, Seger B, Jaramillo TF, Chorkendorff I (2019) Absence of oxidized phases in Cu under CO reduction conditions. ACS Energy Lett 4:803–804. https://doi.org/10.1021/acsenergylett.9b00172

[40] Lum Y, Ager JW (2018) Stability of residual oxides in oxide-derived copper catalysts for electrochemical CO_2 reduction investigated with ^{18}O labeling. Angew Chem Int Ed 57:551–554. https://doi.org/10.1002/anie.201710590

[41] Sacco A (2018) Electrochemical impedance spectroscopy as a tool to investigate the electroreduction of carbon dioxide: a short review. J CO2 Util 27:22–31. https://doi.org/10.1016/j.jcou.2018.06.020

[42] Reid O, Saleh F, Easton E (2013) Determining electrochemically active surface area in PEM fuel cell electrodes with electrochemical impedance spectroscopy and its application to catalyst durability. Electrochim Acta 114:278–284. https://doi.org/10.1016/j.electacta.2013.10.050

[43] Waszczuk P, Zelenay P, Sobkowski J (1995) Surface interaction of benzoic acid with a copper electrode. Electrochim Acta 40:1717–1721. https://doi.org/10.1016/0013-4686(95)00088-V

[44] Qin B, Li Y, Fu H, Wang H, Chen S, Liu Z, Peng F (2018) Electrochemical reduction of CO_2 into tunable syngas production by regulating the crystal facets of earth-abundant Zn catalyst. ACS Appl Mater Interfaces 10:20530–20539. https://doi.org/10.1021/acsami.8b04809

[45] Farkhondehfal MA, Hernández S, Rattalino M, Makkee M, Lamberti A, Chiodoni A, Bejtka K, Sacco A, Pirri FC, Russo N (2019) Syngas production by electrocatalytic reduction of CO_2 using Ag-decorated TiO_2 nanotubes. Int J Hydrog Energy. https://doi.org/10.1016/j.ijhydene.2019.04.180

[46] Lan Y, Gai C, Kenis PJA, Lu J (2014) Electrochemical reduction of carbon dioxide on Cu/CuO core/shell catalysts. ChemElectroChem 1:1577–1582. https://doi.org/10.1002/celc.201402182

[47] Chen K, Zhang X, Williams T, Bourgeois L, MacFarlane DR (2017) Electrochemical reduction of CO_2 on core-shell Cu/Au nanostructure arrays for syngas production. Electrochim Acta 239:84–89. https://doi.org/10.1016/j.electacta.2017.04.019

[48] Wuttig A, Yaguchi M, Motobayashi K, Osawa M, Surendranath Y (2016) Inhibited proton transfer enhances Au-catalyzed CO_2-to-fuels selectivity. PNAS 113:E4585–E4593. https://doi.org/10.1073/pnas.1602984113

[49] Luo W, Zhang J, Li M, Züttel A (2019) Boosting CO production in electrocatalytic CO_2 reduction on highly porous Zn catalysts. ACS Catal 9:3783–3791. https://doi.org/10.1021/acscatal.8b05109

[50] Singh MR, Goodpaster JD, Weber AZ, Head-Gordon M, Bell AT (2017) Mechanistic insights into electrochemical reduction of CO_2 over Ag using density functional theory and transport models. Proc Natl Acad Sci USA 114:E8812–E8821. https://doi.org/10.1073/pnas.1713164114